

## Resolving the microscopic hydrodynamics at the moving contact line

Amal K. Giri <sup>1</sup>, Paolo Maggaretti <sup>1</sup>, Dirk Peschka <sup>2</sup>, and Marcello Sega <sup>1,\*</sup>

<sup>1</sup>*Forschungszentrum Jülich GmbH, Helmholtz Institute Erlangen-Nürnberg for Renewable Energy (IEK-11),  
Cauerstrasse 1, D-91058 Erlangen, Germany*

<sup>2</sup>*Weierstrass Institute Berlin, Mohrenstrasse 39, D-10117 Berlin, Germany*



(Received 30 June 2022; accepted 15 September 2022; published 10 October 2022)

The molecular structure of moving contact lines (MCLs) and the emergence of a corresponding macroscopic dissipation have made the MCL a paradigm of fluid dynamics. Through novel averaging techniques that remove capillary waves smearing we achieve an unprecedented resolution in molecular dynamics simulations and find that they match with the continuum description obtained by finite element method down to molecular scales. This allows us to distinguish dissipation at the liquid-solid interface (Navier-slip) and at the contact line, the latter being negligible for the rather smooth substrate considered.

DOI: [10.1103/PhysRevFluids.7.L102001](https://doi.org/10.1103/PhysRevFluids.7.L102001)

Controlling the properties of moving contact lines (MCLs) is key to many modern technological applications, including printable photovoltaics [1], ink-jet printing [2], liquid-coating and paint-drying processes [3]. However, modeling the MCL is complicated because continuum descriptions often fail to describe the fluids microstructure in its proximity. A naive approach based on the no-slip boundary condition encounters a nonintegrable stress singularity, raising what is known as the Huh-Scriven paradox [4]. Several mechanisms have been proposed to remove the singularity at the MCL present in dynamic wetting [5–8]. Among these mechanisms are, for example, the Cox-Voinov law [9,10], the molecular-kinetic theory [11,12], and the interface formation theory [13,14]. Notably, all these approaches rely on the introduction of a microscopic length scale below which the classical hydrodynamics of a homogeneous, incompressible, Newtonian fluid fails. To extend the applicability of hydrodynamics, additional dissipation mechanisms have been suggested, including Navier-slip [15] and MCL dissipation [16,17]. In addition, this picture is further complicated by the number of physical mechanisms that can contribute to the dissipation at the liquid-solid interface [18,19], including phonons [20,21], electronic excitations [22], and charge build-up [23].

Accordingly, a detailed picture is needed to understand these phenomena at the molecular scale in the MCL region. Molecular dynamics (MD) simulations can deliver a microscopically detailed picture of the MCL [24] and have been successful on many fronts, for example, in evidencing the breakdown of local hydrodynamics [25], providing support for the molecular-kinetic theory both with simple [26] and hydrogen-bonding substrates [27] or investigating the time scale for the liquid-solid tension relaxation [28]. In previous MD studies, the fluid flow at the contact line was affected by evaporation [29] and significant contact line dissipation emerged from strong hydrogen bonding at the liquid-solid interface [30], neither of which plays a role in our work.

Despite the potential for providing information at the molecular scale, the presence of thermal capillary waves [31] is setting a limit to the resolution one can achieve close to the liquid-vapor interface. Capillary wave theory [32] predicts that spontaneous surface excitations broaden the width of fluid interfaces with a logarithmic divergence that depends on the simulation cell size. For small

---

\*m.sega@ucl.ac.uk; Present address: Department of Chemical Engineering, University College London, London WC1E 7JE, United Kingdom.

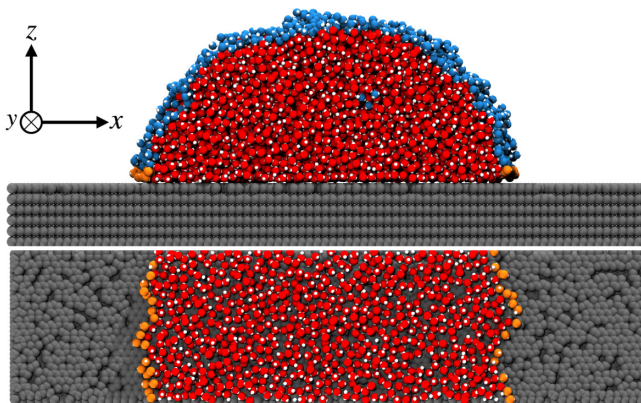


FIG. 1. MD snapshot of a cylindrical droplet with 7332 water molecules in a box  $L_x \times L_y \times L_z = 198.9 \text{ \AA} \times 46.8 \text{ \AA} \times 170 \text{ \AA}$  and external acceleration of  $5 \times 10^{-3} \text{ \AA/ps}^2$  along the  $x$  direction. Red: oxygen atoms; blue: oxygen atoms at the liquid-vapor interface; orange: oxygen atoms at the MCL; gray: carbon atoms of the substrate. Top: side view; bottom: top view of the first water layer

molecular liquids and typical simulation cells, these fluctuations are larger than the molecular size [31,33] at room temperature. Several computational strategies have been devised to recover the intrinsic structure of fluid interfaces [33–39]. In some of these, including the approach reported here, one first identifies molecules at the phase interface as shown in Fig. 1, then uses them to define a local coordinate system. In turn, one can use this coordinate system to compute the profiles of chosen observables as a function of the local distance from the interface. To obtain further insight into the dynamics of the molecules at the MCL, one has to cope with its fluctuations. In this case, however, two interfaces are involved (liquid-vapor and liquid-solid), and one-dimensional intrinsic profiles are not enough to describe the system. Here, we extend the approach of intrinsic profiles to the region around the three-phase contact line by introducing two-dimensional density maps that are functions of the position relative to the liquid-vapor and liquid-solid interfaces, respectively. This procedure allows us to resolve the structure and the flow close to the MCL at an unprecedented resolution.

We performed MD simulations of a cylindrical water droplet moving on a rigid substrate under the influence of a constant acceleration parallel to the solid surface. Water is modeled using the SPC/E potential [40] and the substrate as a rigid, graphite-like structure with defects [41], obtained by removing 35% of randomly selected surface atoms. The presence of defects serves rather well the purpose of providing a friction coefficient thanks to the lateral modulation of the water-surface interaction potential. All molecular dynamics simulations are performed with an in-house modified version of the GROMACS simulation package, release 2019.4 [42], that uses a Nosé-Hoover [43,44] thermostat coupled only to the direction orthogonal to both the surface normal and the external force [25], keeping in mind that this introduces a bias in the surface energies [45]. Further details are reported in the Supplemental Material [46]. This includes details on all the algorithms used [47–52]. Input files and GROMACS source code patch are provided in a dataset available on Zenodo [53].

The first step in computing intrinsic maps of the droplet’s hydrodynamic fields is identifying the surface molecules at the liquid-vapor interface, cf. Fig. 1. Here, as detailed in the Supplemental Material [46], we use the GITIM algorithm [39] as implemented in the Pytim package [50]. The surface molecules are used to provide the location of the (continuum) liquid-vapor  $\zeta_V(\mathbf{r})$  and liquid-solid  $\zeta_S(\mathbf{r})$  interfaces by using a linear interpolation between neighboring triplets of surface molecules. We compute the intrinsic map of a generic local observable  $A$  as  $A(\xi) = \langle \sum_i A_i \prod_\alpha \delta(\xi_\alpha - \min |r_i - \zeta_\alpha|) \rangle / N(\xi)$ . Here,  $\alpha = \{V, S\}$  labels the liquid-vapor and liquid-solid interfaces and  $\xi = (\xi_V, \xi_S)$  are the distances of a point in space from the two surfaces. The angular brackets indicate a statistical average over time, and the index  $i$  labels particles. The normalization factor  $N(\xi)$  is calculated from the intrinsic density map of uniformly distributed random points

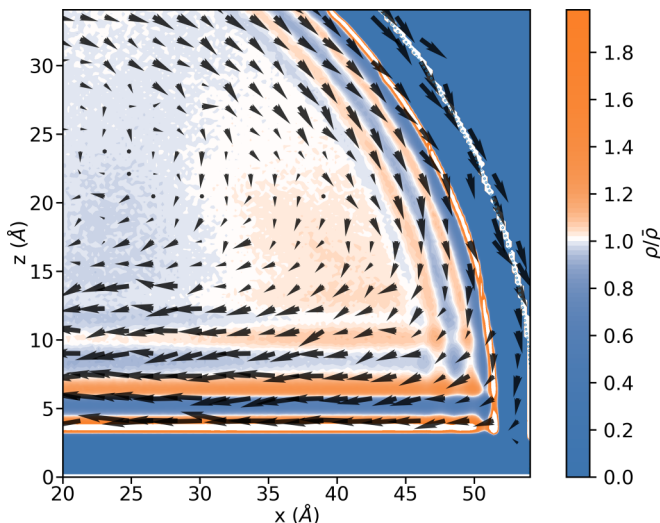


FIG. 2. Intrinsic map of the density (color) and velocity field in the comoving reference frame (arrows). The molecules belonging to the liquid-vapor interface have zero inherent distance  $\xi_V$  and are represented here using the result of an elliptic fit through their average position (small open circles). The density field has resolution  $0.22 \text{ \AA} \times 0.2 \text{ \AA}$  and is normalized with respect to the bulk density. The velocity field has resolution  $1.7 \text{ \AA} \times 1.6 \text{ \AA}$  and is scaled such that an arrow of length  $1 \text{ \AA}$  on the plot corresponds to a velocity of  $0.01 \text{ \AA/ps}$ .

within the liquid phase. The two-dimensional intrinsic map  $A(\xi)$  is best interpreted if remapped back from the generalized coordinates  $(\xi_V, \xi_S)$  to the Cartesian ones using the average location of the interfaces as the origin of the local frame. This approach provides precise information close to the liquid-vapor interface but loses accuracy far away from the interface. However, this region is not of concern for the current investigation, which focuses on the neighborhood of the MCL. The intrinsic density field reported in Fig. 2 reveals the oscillations associated to molecular layering at both the liquid-solid and liquid-vapor interfaces. In particular, a pronounced gap region due to hard-core repulsion appears next to both interfaces. As shown in Fig. 2, the resolution of the velocity field matches the molecular scale, with bins of size  $1.7 \text{ \AA} \times 1.6 \text{ \AA}$ , while the density bins are of size  $0.22 \text{ \AA} \times 0.2 \text{ \AA}$ . We do not observe any trace of an influence of positional correlations on the velocity field, which is a much smoother function of the position than the density. It is often remarked that continuum hydrodynamics breaks down in simple liquids below scales of few molecular diameters [54,55]. However, this is true for processes like sound propagation that, at that scale, happen during extremely short times on the order of a picosecond. In contrast, we compute the stationary fields of the hydrodynamic quantities by averaging over time intervals so large that no memory effect can survive.

The density map is in fact a correlation function and the oscillations can be interpreted as in a pair correlation function. The local density, computed as the (reciprocal) average volume available for each atom, is constant over the whole liquid phase and the droplet is incompressible (see plot of  $\nabla \cdot \mathbf{v}$  in Fig. A8 of the Supplemental Material [46]) down to and below the molecular scale. Therefore, the stationary velocity field that we compute from MD data can be modeled as that of a homogeneous incompressible fluid in the finite element method (FEM) simulations.

In Fig. 3 we report the horizontal velocity profile for molecules in the slab  $z < 6 \text{ \AA}$ , computed in the droplet comoving frame using both the global and intrinsic coordinate systems. The velocity sampled in the global coordinate system extends further than the intrinsic one because of the fluctuations. Both profiles coincide in the region  $|x| < 50 \text{ \AA}$ , showing a steep increase when departing from the droplet center. However, close to the MCL, the velocity profile computed in the global coordinate system flattens out. In contrast, the intrinsic one is compatible over its entire

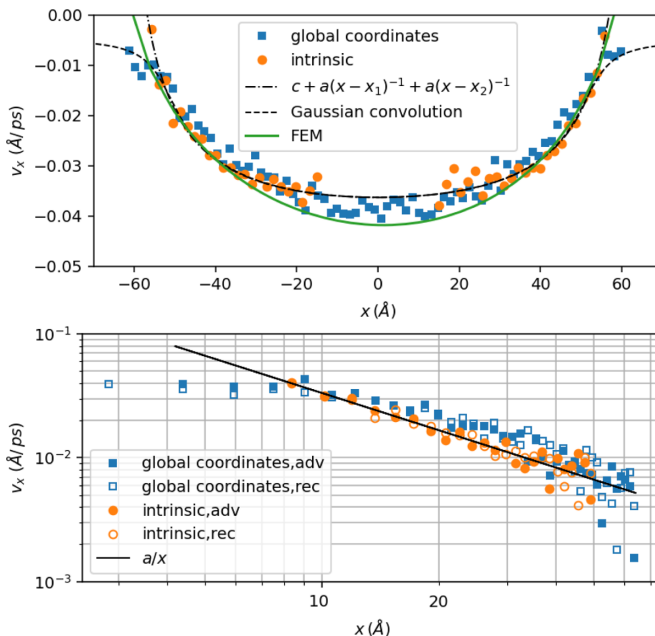


FIG. 3. Top panel: horizontal velocity profiles (squares: global coordinate system; circles: intrinsic profiles) sampled along  $x$  at  $z = 3 \pm 3 \text{ \AA}$ . The dot-dashed curve is a fit to a power law  $c + a(x - x_1)^{-1} + a(x_2 - x)^{-1}$ . The dashed line is the convolution of the best-fit power law with a Gaussian as described in the text ( $a = -0.435 \text{ \AA}^2/\text{ps}$ ,  $c = -0.0495 \text{ \AA}/\text{ps}$ ,  $x_1 = 66.42 \text{ \AA}$ ,  $x_2 = -66.33 \text{ \AA}$ ). The green curve is the FEM solution evaluated at the interface  $z = 0$ . Bottom panel: double logarithmic scale, same data as in the top panel but symmetrized along the vertical axis and shifted so that the fitting constants  $c$  and  $x_1$  are zero ( $a = 0.335 \text{ \AA}^2/\text{ps}$ ).

extension with a power-law slip profile. The profile in the global coordinate system can be very well described in the spirit of the capillary wave theory by using quantities  $\tilde{A}(x) = \int_0^{L_x} G(x - x')A(x')dx'$  convoluted with the Gaussian distribution  $G(x) \sim \exp[-x^2/(2\sigma^2)]$  of the interface fluctuations, so that  $v_x = \tilde{p}_x/\tilde{\rho}$ . Here,  $A(x)$  is the profile of observable  $A$  averaged over the whole range in  $y$  direction and over the first molecular layer in the  $z$  direction.

In the top panel of Fig. 3 we report as a dashed-line the velocity profile obtained by applying this convolution procedure to the best fit intrinsic velocity profile  $v_x \sim (x - x_1)^{-1} + (x_2 - x)^{-1}$  and a steplike density profile, using the interfacial layer width  $\sigma = 2.5 \text{ \AA}$ . The resulting profile reproduces very well the flattening in the region close to the MCL. These features are more evident in the double logarithmic scale, reported in the right panel of Fig. 3, where we have symmetrized the profile around its minimum and shifted it vertically and horizontally by the fitting constants  $x_1$  and  $c$ . Our results show that after removing the capillary fluctuations via the intrinsic map method, the power-law behavior extends over the entire range down to the molecular length scale, and the previously reported departure from the power law [56] is due to the smearing introduced by capillary waves rather than a breakdown of hydrodynamics at short length scales.

The present computational approach allows us to discuss some of the proposed corrections to continuum models. We compare our MD simulation results with a full hydrodynamic continuum model for the MCL, where we solve a Stokes problem for an incompressible viscous Newtonian fluid ( $\text{Re} = 0$ ) featuring a free interface subject to capillary forces, which is driven by a constant acceleration  $\mathbf{g}$ . Dissipative processes are included by the combination of Navier-slip, i.e.,  $\beta u_x = \mu \partial_z u_x$ , and dynamic contact line dissipation [57], i.e.,  $v_x u_x = \gamma/\delta(\cos \theta_e - \cos \theta)$ . The slip parameter  $\beta$  enhances the inhomogeneity in the flow by increasing  $\partial_z u_x$ . In contrast, the contact line friction  $\delta$  enhances the asymmetry of the droplet shape through advancing and receding contact angle, e.g.,

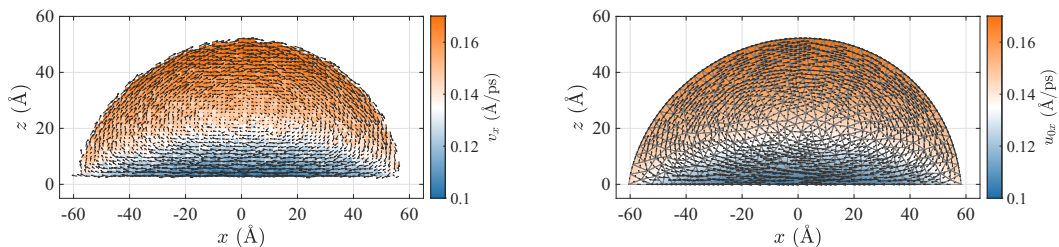


FIG. 4. Left: averaged MD velocity profile  $\mathbf{v} = (v_x, v_z)$  (shown for  $\rho > 0.66\bar{\rho}$ ); right: optimal Stokes velocity profile  $\mathbf{u}_0 = (u_{0x}, u_{0z})$  for  $\beta = 1.38$  (slip-length  $b = 40\text{\AA}$ ) and  $\delta = 0$ ,  $\text{Bo} = 0.2414$  and  $\vartheta_e = 97.2^\circ$  in a comoving frame (vectors) and absolute horizontal velocity (shading).

cf. Fig. A5 of the Supplemental Material [46]. Note that we use constant slip length and contact line dissipation, as space-dependent coefficients would yield an overdetermined improved fit but not lead to new physical insights. We discretize the system of partial differential equations using the isoparametric  $\mathbf{P}_2 - \mathbf{P}_1$  Taylor-Hood finite elements combined with an ALE mesh motion strategy, for details cf. the Supplemental Material [46] and Refs. [58,59].

For a given acceleration  $\mathbf{g}$  and droplet size  $L$ , we compare the velocity of traveling-wave solutions from the Stokes problem  $\mathbf{u}(t, \mathbf{r}) = \mathbf{u}_0(x - v_0 t, z)$  with the corresponding velocity from the MD problem by computing the root-mean-square deviation (rmsd)  $\Delta$ , relative to the MD accuracy, with  $\Delta^2 = \int_{\Omega_0} \rho |\mathbf{u}_0 - \mathbf{v}|^2 / \delta v^2 dx dz / \int_{\Omega} \rho dx dz$ , in the comoving frame  $\Omega_0 = \Omega - (v_0, 0)t$ , where  $\delta \mathbf{v}(x, z)$  is the space-dependent MD averaging error of  $\mathbf{v}$ . In Fig. 4 we show the excellent agreement of the horizontal components of MD and Stokes velocity for a droplet with optimized  $\beta$  and  $\delta$ . Correspondingly, in Fig. 5 we show the rmsd  $\Delta$  for different pairs of  $\delta$  and  $\beta$ , where the optimal parameters suggest a vanishing or small contact line dissipation  $0 < \delta < 0.05$  and  $\beta = 1.38$ , corresponding to a slip-length  $b = 40\text{\AA}$ . Because  $\Delta$  is a relative measure of inaccuracy with respect to that of MD, we expect  $\Delta \sim \mathcal{O}(1)$  for a good fit, similarly to a reduced  $\chi^2$  test. For given  $\delta$ , the local minima in Fig. 5 suggest that also other parameters with larger  $\delta$  and smaller  $\beta$  are feasible. However, those parameters are not optimal for the prescribed bulk viscosity  $\mu = 0.7\text{ mPa s}$  but could possibly be improved by fitting the entire triple  $(\mu, \beta, \delta)$ , considering spatially inhomogeneous parameters or a compressibility of the fluid.

The water molecules are subjected to a friction force that, in steady-state conditions, balances  $\mathbf{g}$  and is defined as the horizontal component of the force density  $f_{\Gamma,x}(x, z)$  acting from the substrate on water molecules. Even though long-range corrections for dispersion forces are in place, the friction force becomes negligible at larger elevations  $z \gtrsim 10\text{\AA}$  and is acting almost exclusively on the first

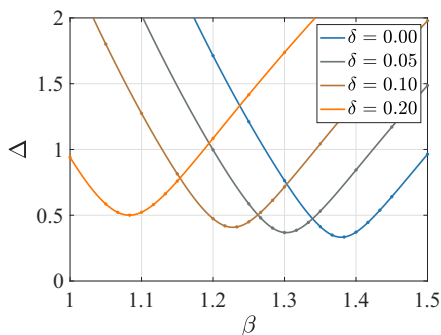


FIG. 5. Rmsd  $\Delta$  between FEM and MD flow fields for different dissipation parameters  $\beta$  (Navier-slip) and  $\delta$  (contact line) in the hydrodynamic Stokes model.

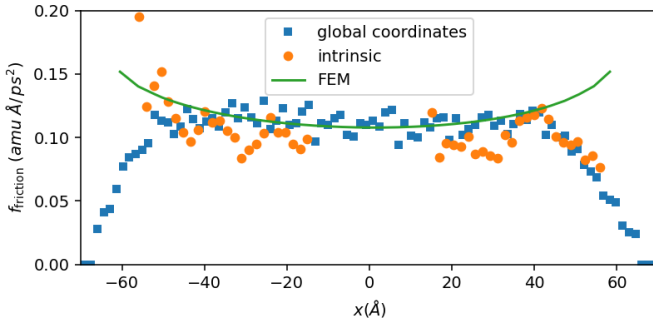


FIG. 6. Profile of the friction surface density computed from the MD data in the global (squares) and intrinsic (circles) coordinate systems. The green curve is the FEM solution evaluated at the interface  $z = 0$ .

layer of water molecules at the substrate. Therefore, we can define a friction force per unit area as  $F_{\Gamma}(x) = \int_0^{\infty} f_{\Gamma,x}(x, z) dz$ . This force is the counterpart of the surface friction that in sharp interface models like the present FEM can be calculated from the stress  $\mathbf{t} \cdot \boldsymbol{\sigma} \mathbf{v} \equiv -\mu_{\Gamma} \mathbf{t} \cdot \mathbf{u}$  at the solid-liquid interface, where  $\mathbf{t}$  and  $\mathbf{v}$  are the corresponding tangential and normal vectors. Figure 6 shows the friction surface density  $F_{\Gamma}$  obtained from the MD trajectories and compared to the FEM results. Far from the droplet edges, both force profiles are in excellent agreement. However, close to the advancing and receding MCL, the friction force behaves qualitatively differently. This mismatch contrasts the overall good match of the slip velocity profile Fig. 3. Therefore, even though the Navier-slip boundary condition is an excellent effective model in reproducing the slip velocity, the same is not true concerning the friction force near the MCL.

This difference implies that the underlying dynamics is more complex than that encoded into the Navier-slip boundary condition. Remarkably, even in the present case, where the substrate is particularly smooth and the optimal FEM solution is compatible with zero contact line dissipation, we observe a significant deviation of the friction force from the one emerging from the Navier-slip boundary condition. Note that, upon integration of the force density in Fig. 6, this contribution is compatible with a contact line friction  $\delta \lesssim 0.05$ . Larger defects or soft substrates will enhance this effect.

In this work, we compared microscopic MD simulations and hydrodynamic FEM simulations of sliding droplets with respect to their densities, flow and force fields at interfaces and MCLs. Using a novel averaging method, we showed that assumptions of continuum hydrodynamics are valid near the MCL. However, despite an effectively vanishing contact line friction, corrections to the force balance are clearly visible. In the future, larger droplets or elastic substrates with stronger roughness should be investigated to further enhance contact line friction and suppress density oscillations. Additionally, one should consider thermodynamics, compressibility, and evaporation of the liquid phase to better match continuum hydrodynamics with the microscopic interacting-particle system.

The datasets available on Zenodo [53] provide MD input files, the GROMACS source code patch for the thermostat, averaged data from MD simulations (Cartesian mesh with mass density and velocity field) as well as FEM simulation solutions (triangular 2D droplet mesh with velocity field) in ASCII format, and MATLAB functions for the data import and plot generation. The MATLAB code is available at Ref. [60].

#### ACKNOWLEDGMENTS

D.P., A.K.G., and M.S. acknowledge the funding by the German Research Foundation (DFG) through the Projects No. 422792530 (D.P.) and No. 422794127 (A.K.G. and M.S.) within the DFG Priority Program SPP 2171 *Dynamic Wetting of Flexible, Adaptive, and Switchable Substrates*.

- 
- [1] J. J. Berry, J. van de Lagemaat, M. M. Al-Jassim, S. Kurtz, Y. Yan, and K. Zhu, Perovskite photovoltaics: The path to a printable terawatt-scale technology, *ACS Energy Lett.* **2**, 2540 (2017).
- [2] M. Singh, H. M. Haverinen, P. Dhagat, and G. E. Jabbour, Inkjet printing—Process and its applications, *Adv. Mater.* **22**, 673 (2010).
- [3] R. D. Deegan, O. Bakajin, T. F. Dupont, G. Huber, S. R. Nagel, and T. A. Witten, Contact line deposits in an evaporating drop, *Phys. Rev. E* **62**, 756 (2000).
- [4] C. Huh and L. E. Scriven, Hydrodynamic model of steady movement of a solid/liquid/fluid contact line, *J. Colloid Interface Sci.* **35**, 85 (1971).
- [5] C. Neto, D. R. Evans, E. Bonaccorso, H.-J. Butt, and V. S. J. Craig, Boundary slip in Newtonian liquids: A review of experimental studies, *Rep. Prog. Phys.* **68**, 2859 (2005).
- [6] D. Bonn, J. Eggers, J. Indekeu, J. Meunier, and E. Rolley, Wetting and spreading, *Rev. Mod. Phys.* **81**, 739 (2009).
- [7] J. H. Snoeijer and B. Andreotti, Moving contact lines: Scales, regimes, and dynamical transitions, *Annu. Rev. Fluid Mech.* **45**, 269 (2013).
- [8] G. Lu, X.-D. Wang, and Y.-Y. Duan, A critical review of dynamic wetting by complex fluids: From Newtonian fluids to non-Newtonian fluids and nanofluids, *Adv. Colloid Interface Sci.* **236**, 43 (2016).
- [9] O. V. Voinov, Hydrodynamics of wetting, *Fluid Dyn.* **11**, 714 (1977).
- [10] R. G. Cox, The dynamics of the spreading of liquids on a solid surface. Part 1. Viscous flow, *J. Fluid Mech.* **168**, 169 (1986).
- [11] T. D. Blake and J. M. Haynes, Kinetics of liquid-liquid displacement, *J. Colloid Interface Sci.* **30**, 421 (1969).
- [12] T. D. Blake and J. De Coninck, The influence of solid–liquid interactions on dynamic wetting, *Adv. Colloid Interface Sci.* **96**, 21 (2002).
- [13] Y. D. Shikhmurzaev, Moving contact lines in liquid/liquid/solid systems, *J. Fluid Mech.* **334**, 211 (1997).
- [14] Y. D. Shikhmurzaev, The moving contact line on a smooth solid surface, *Int. J. Multiphase Flow* **19**, 589 (1993).
- [15] E. Lauga, M. Brenner, and H. Stone, Microfluidics: The no-slip boundary condition, in *Springer Handbooks* (Springer, Berlin, 2007), pp. 1219–1240.
- [16] M. J. De Ruijter, J. De Coninck, and G. Oshanin, Droplet spreading: Partial wetting regime revisited, *Langmuir* **15**, 2209 (1999).
- [17] P. G. de Gennes, Wetting: Statics and dynamics, *Rev. Mod. Phys.* **57**, 827 (1985).
- [18] M. H. Müser, M. Urbakh, and M. O. Robbins, Statistical mechanics of static and low-velocity kinetic friction, in *Advances in Chemical Physics*, edited by I. Prigogine and Stuart A. Rice (John Wiley & Sons, Hoboken, NJ, 2003), pp. 187–272.
- [19] J. Krim, Friction and energy dissipation mechanisms in adsorbed molecules and molecularly thin films, *Adv. Phys.* **61**, 155 (2012).
- [20] M. Cieplak, E. D. Smith, and M. O. Robbins, Molecular origins of friction: The force on adsorbed layers, *Science* **265**, 1209 (1994).
- [21] M. S. Tomassone, J. B. Sokoloff, A. Widom, and J. Krim, Dominance of Phonon Friction for a Xenon Film on a Silver (111) Surface, *Phys. Rev. Lett.* **79**, 4798 (1997).
- [22] M. S. Tomassone and A. Widom, Electronic friction forces on molecules moving near metals, *Phys. Rev. B* **56**, 4938 (1997).
- [23] T. A. L. Burgo, C. A. Silva, L. B. S. Balestrin, and F. Galembeck, Friction coefficient dependence on electrostatic tribocharging, *Sci. Rep.* **3**, 2384 (2013).
- [24] T. Qian, X.-P. Wang, and P. Sheng, Molecular scale contact line hydrodynamics of immiscible flows, *Phys. Rev. E* **68**, 016306 (2003).
- [25] P. A. Thompson and M. O. Robbins, Simulations of Contact-Line Motion: Slip and the Dynamic Contact Angle, *Phys. Rev. Lett.* **63**, 766 (1989).
- [26] E. Bertrand, T. D. Blake, and J. De Coninck, Influence of solid–liquid interactions on dynamic wetting: A molecular dynamics study, *J. Phys.: Condens. Matter* **21**, 464124 (2009).

- [27] U. Lācis, P. Johansson, T. Fullana, B. Hess, G. Amberg, S. Bagheri, and S. Zaleski, Steady moving contact line of water over a no-slip substrate: Challenges in benchmarking phase-field and volume-of-fluid methods against molecular dynamics simulations, *Eur. Phys. J.: Spec. Top.* **229**, 1897 (2020).
- [28] A. V. Lukyanov and A. E. Likhthman, Relaxation of surface tension in the liquid–solid interfaces of Lennard-Jones liquids, *Langmuir* **29**, 13996 (2013).
- [29] J. B. Freund, The atomic detail of a wetting/de-wetting flow, *Phys. Fluids* **15**, L33 (2003).
- [30] P. Johansson and B. Hess, Molecular origin of contact line friction in dynamic wetting, *Phys. Rev. Fluids* **3**, 074201 (2018).
- [31] J. S. Rowlinson and B. Widom, *Molecular Theory of Capillarity* (Dover Publications, Mineola, NY, 2002).
- [32] F. P. Buff, R. A. Lovett, and F. H. Stillinger, Jr, Interfacial Density Profile for Fluids in the Critical Region, *Phys. Rev. Lett.* **15**, 621 (1965).
- [33] E. Chacón and P. Tarazona, Intrinsic Profiles Beyond the Capillary Wave Theory: A Monte Carlo Study, *Phys. Rev. Lett.* **91**, 166103 (2003).
- [34] A. Werner, F. Schmid, M. Müller, and K. Binder, Anomalous size-dependence of interfacial profiles between coexisting phases of polymer mixtures in thin-film geometry: A Monte Carlo simulation, *J. Chem. Phys.* **107**, 8175 (1997).
- [35] A. Werner, F. Schmid, M. Müller, and K. Binder, “Intrinsic” profiles and capillary waves at homopolymer interfaces: A Monte Carlo study, *Phys. Rev. E* **59**, 728 (1999).
- [36] M. Jorge and M. N. D. S. Cordeiro, Intrinsic structure and dynamics of the water/nitrobenzene interface, *J. Phys. Chem. C* **111**, 17612 (2007).
- [37] L. B. Pártay, G. Hantal, P. Jedlovsky, Á. Vincze, and G. Horvai, A new method for determining the interfacial molecules and characterizing the surface roughness in computer simulations. Application to the liquid–vapor interface of water, *J. Comput. Chem.* **29**, 945 (2008).
- [38] A. P. Willard and D. Chandler, Instantaneous liquid interfaces, *J. Phys. Chem. B* **114**, 1954 (2010).
- [39] M. Sega, S. S. Kantorovich, P. Jedlovsky, and M. Jorge, The generalized identification of truly interfacial molecules (ITIM) algorithm for nonplanar interfaces, *J. Chem. Phys.* **138**, 044110 (2013).
- [40] H. J. C. Berendsen, J. R. Grigera, and T. P. Straatsma, The missing term in effective pair potentials, *J. Phys. Chem.* **91**, 6269 (1987).
- [41] M. Sega, M. Sbragaglia, L. Biferale, and S. Succi, Regularization of the slip length divergence in water nanoflows by inhomogeneities at the Angstrom scale, *Soft Matter* **9**, 8526 (2013).
- [42] M. J. Abraham, T. Murtola, R. Schulz, S. Páll, J. C. Smith, B. Hess, and E. Lindahl, GROMACS: High performance molecular simulations through multi-level parallelism from laptops to supercomputers, *SoftwareX* **1-2**, 19 (2015).
- [43] S. Nosé, A molecular dynamics method for simulations in the canonical ensemble, *Mol. Phys.* **52**, 255 (1984).
- [44] W. G. Hoover, Canonical dynamics: Equilibrium phase-space distributions, *Phys. Rev. A* **31**, 1695 (1985).
- [45] M. Sega and P. Jedlovsky, The impact of tensorial temperature on equilibrium thermodynamics, *Phys. Chem. Chem. Phys.* **20**, 16910 (2018).
- [46] See Supplemental Material at <http://link.aps.org/supplemental/10.1103/PhysRevFluids.7.L102001> for details on the MD and FEM simulations, effect of droplet size, slip length and contact line dissipation on the flow, density and velocity of the liquid-vapor surface layer, and compressibility map.
- [47] S. Miyamoto and P. A. Kollman, Settle: An analytical version of the SHAKE and RATTLE algorithm for rigid water models, *J. Comput. Chem.* **13**, 952 (1992).
- [48] U. Essmann, L. Perera, M. L. Berkowitz, T. Darden, H. Lee, and L. G. Pedersen, A smooth particle mesh Ewald method, *J. Chem. Phys.* **103**, 8577 (1995).
- [49] N. Michaud-Agrawal, E. J. Denning, T. B. Woolf, and O. Beckstein, MDAnalysis: A toolkit for the analysis of molecular dynamics simulations, *J. Comput. Chem.* **32**, 2319 (2011).
- [50] M. Sega, G. Hantal, B. Fábíán, and P. Jedlovsky, Pytim: A python package for the interfacial analysis of molecular simulations, *J. Comput. Chem.* **39**, 2118 (2018).
- [51] I. Shvab and R. J. Sadus, Intermolecular potentials and the accurate prediction of the thermodynamic properties of water, *J. Chem. Phys.* **139**, 194505 (2013).

- [52] M. Sega and C. Dellago, Long-range dispersion effects on the water/vapor interface simulated using the most common models, *J. Phys. Chem. B* **121**, 3798 (2017).
- [53] A. K. Giri, P. Malgaretti, D. Peschka, and M. Sega, dataset for “Resolving the microscopic hydrodynamics at the moving contact line”, Zenodo 706651, doi: [10.5281/zenodo.706651](https://doi.org/10.5281/zenodo.706651) (2022).
- [54] C.-H. Chung and S. Yip, Generalized hydrodynamics and time correlation functions, *Phys. Rev.* **182**, 323 (1969).
- [55] N. K. Ailawadi, A. Rahman, and R. Zwanzig, Generalized hydrodynamics and analysis of current correlation functions, *Phys. Rev. A* **4**, 1616 (1971).
- [56] T. Qian, X.-P. Wang, and P. Sheng, Power-Law Slip Profile of the Moving Contact Line in Two-Phase Immiscible Flows, *Phys. Rev. Lett.* **93**, 094501 (2004).
- [57] W. Ren and W. E, Boundary conditions for the moving contact line problem, *Phys. Fluids* **19**, 022101 (2007).
- [58] D. Peschka, Variational approach to dynamic contact angles for thin films, *Phys. Fluids* **30**, 082115 (2018).
- [59] F. Montefusco, F. S. Sousa, and G. C. Buscaglia, High-order ALE schemes for incompressible capillary flows, *J. Comput. Phys.* **278**, 133 (2014).
- [60] D. Peschka, A MATLAB solver for Stokes free boundary problem, (2022), <https://github.com/dpeschka/stokes-free-boundary>.